Supporting Information

Deep Defect Passivating and Shallow Vacancy Repairing via Ionic Silicone Polymer toward Highly Stable Inverted Perovskite Solar Cells

Tong Wang [a], Yuke Li [b], Qi Cao [a], Jiabao Yang [a], Bowen Yang [c,d], Xingyu Pu [a], Youzi Zhang [a], Junsong Zhao [a], Yixin Zhang [a], Hui Chen [a], Anders Hagfeldt [c,d], Xuanhua Li [a,*]

[a] State Key Laboratory of Solidification Processing, Center for Nano Energy Materials, School of Materials Science and Engineering, Northwestern Polytechnical University, Xi´an 710072, China

[b] Department of Chemistry and Centre for Scientific Modeling and Computation, Chinese University of Hong Kong, Shatin, Hong Kong, China

[c] Department of Chemistry-Ångström Laboratory, Uppsala University, SE-75120 Uppsala, Sweden

[d] Laboratory of Photomolecular Science, Institute of Chemical Sciences and Engineering, School of Basic Sciences, Ecole Polytechnique Fédérale de Lausanne, CH-1015 Lausanne, Switzerland

* Mail address: lixh32@nwpu.edu.cn

Experimental Section

Materials

The solvents and chemicals were purchased commercially and used without further purification (except where noted). FAI, CsI, MABr, $PbBr_2$, PbI_2, PCBM, $C_{60,}$ and BCP were obtained from Xi'an Polymer Light Technology Corp. Chlorobenzene (CB, 99.8%), isopropanol (IPA, 99.9%), anhydrous dimethyl sulfoxide (DMSO, 99.8%), N, N-dimethylformamide (DMF, 99.8%), and nickel (II) nitrate hexahydrate (Ni $(NO_3)_2 \cdot 6H_2O$, 99.999%) were purchased from Sigma-Aldrich. The BTMC and the raw materials for synthetic polymers were purchased from Shanghai Macklin Biochemical Technology Corp. The NiO_x nanoparticles were synthesized based on previous reports.[1]

Synthesis of PEDE and PECL

1,3-diglycidyl ether oxypropyl (1,1,3,3-tetramethyl) tetrasiloxane (3.56 g) and amino-terminated polyethylene glycol (2.00 g) were added in a three-necked flask with the stirring rod and thermometer. Isopropanol was chosen as the solvent. The reaction was conducted at 85 °C for 3 h to obtain a polyether-modified epoxy end-capping agent. After the system cooled to room temperature, adding octa-methyl cyclo tetra siloxane (5.92 g) and tetramethylammonium hydroxide (0.09 g) as the catalyst for the reaction system. After the temperature was raised to 75 °C, the vacuum distillation was conducted for 40 min, and the reaction was continued at 95 °C for 30 min to obtain the block copolymer PEDE. To obtain the PECL, the polyether-modified epoxy end-capping agent (1.50 g), octa-methyl cyclo tetra siloxane (1.48 g), trimethyl-3-(trimethoxysilyl) propylammonium chloride (2.20 g), and tetramethylammonium hydroxide (0.14 g) were added in a three-necked flask. After the vacuum distillation, the reaction was heated to 80 ℃ for 2 h to obtain the ionic silicone polymer.

Device Fabrication

ITO glasses were rinsed with deionized water, acetone, and ethyl alcohol, respectively. After being treated with UV ozone plasma for 15 min, NiO_x (20 mg ml^{-1}) was spin-coated on the cleaned substrates at 3000 rpm for the 30 s and heated at 100 °C for 10 min. We mixed the $PbBr_2$ (0.21 M), PbI_2 (1.30 M), MABr (0.21 M), FAI (1.19 M), and CsI (0.07 M) in DMSO/DMF (1/4 V/V) and stirred overnight. The perovskite precursor solution of $Cs_{0.05}(MA_{0.15}FA_{0.85})_{0.95}Pb(I_{0.85}Br_{0.15})_3$ was spin-coated onto NiO_x film at speed of 1000 rpm for 10 s and 6000 rpm for 30 s. The anti-solvent chlorobenzene (CB) with different concentrations of additives was added after 20 s. The ITO glasses were transferred to a heating platform and baked at 100 °C for 20 min. After the substrates were cooled to room temperature, the PCBM and C_{60} mixed solution (25 mg mL^{-1}, 4/1, w/w) was spin-coated at speed of 4000 rpm for 50 s. Then, the BCP solution (0.5 mg mL^{-1}) was spin-coated at speed of 5000 rpm for 40 s and annealed at

60 °C for 20 min. Finally, the Cr (4 nm) and Au (100 nm) were evaporated respectively by vacuum evaporation equipment at 2×10^{-6} mbar (0.1 cm^2 effective area).

Perovskite Film Characterizations

The Fourier transform infrared spectroscopy (FTIR) spectra were measured by FTIR-6100 (Jasco) with a range from 4000 cm^{-1} to 600 cm^{-1}. The X-ray photoelectron spectroscopy (XPS) was obtained by Kratos instrument (Axis Supra) with the source of Al Kα. The UPS measurements were also carried out on a Kratos instrument (Axis Supra), with the HeI (21.22 eV) emission line employed for excitation. ^{1}H NMR spectra were tested by the Bruker AVANCE 600 MHz, deuterated DMSO was used as the solvent. The molecular weight of polymers was measured via gel permeation chromatography (Waters 1515, tetrahydrofuran as the mobile phase). The top-view and cross-section SEM images of perovskite films were performed by SEM (FEI, Verios G4) under 10 kV applied bias. The TEM images were obtained with a FEI Talos F200X operating on 200 kV electron gun. The perovskite is scraped from the substrates and collected 5 mg of powder for each sample. Then, the powder is dispersed in chlorobenzene and sonicated for one hour. The XRD spectra of films were obtained by Cu Kα (Kratos, XRD-7000) from 5° to 60° with the speed of 5°/min. The ultraviolet-visible (UV-vis) absorption spectra were performed by the spectrophotometer (Lambda 35, Perkin-Elmer) with the range of 300 nm-850 nm. The steady-state PL spectra were obtained by Edinburgh FLS980 spectrometer with an emission wavelength of 480 nm. PLQE measurements were carried out inside an integrating sphere (Labsphere). The TRPL spectra were performed by the FLS920 fluorescence spectrometer (Edinburgh Instruments). The change of light absorption during the spin-coating process of perovskite film was studied by self-made in-situ light absorption device.[2]

Device Characterizations

The devices under AM 1.5G illumination (Newport 94023A Oriel Sol3A, Class AAA, 100 mW/cm^2, the light intensity was calibrated by standard silicon diode (Hamamatsu S1133)) were tested via the Keithley source meter (2420) with the scanning speed of 0.1 V/s for obtaining the J-V curves. EQE spectra of the PSCs were obtained from QE-R3011 (Enli Tech) using Czerny-Turner monochromatic incident light. EIS was conducted by an electrochemical workstation (Chenhua760, China) with a bias voltage of 0.8 V, and the frequency range is 1 MHz to 0.1 Hz. The thermal admittance spectroscopy was conducted by the ZAHNER electrochemical workstation (Zennium-E) at various temperatures (T= 278–318 K) in the dark from 100 to 10^6 Hz. Temperatures were regulated by the temperature controller (Oxford Instruments, ITC 502) under vacuum conditions (< 5 mbar). The Mott Schottky analysis was also obtained by the device with the 1kHz AC frequency and 0-1.5 V bias. According to the Mott

Schottky curves, the tDOS were obtained via the curve of frequency-dependent capacitance. We used UV adhesive (LT-U001, Lumtec) to encapsulate the devices in the N_2 glove box. The encapsulated devices were aged in LED lamp light-soaking (AM 1.5 G, 100 mW/cm^2) with a sixteen-channel thin film photovoltaic maximum power point tracking test system (YH-VMPP-16) for operational stability test. we placed the unencapsulated PSCs on a hot plate at 85 °C in the N_2 glove box to obtain the thermal stability measurement per week.

Quantum Chemical Calculations

Density functional theory (DFT) calculations were conducted by using the B3LYP functional and the all-electron double-ξ valence basis sets with polarization functions 6-31G* (B3LYP/6-31G*). The calculation process was implemented in the Gauss 09 program. Geometry optimizations of the ionic groups were performed with full relaxation of all atoms without solvent effects.[3]

Density functional theory Calculation

Since FA as a cation and I as an anion are the most abundant species in the experimentally studied $Cs_{0.05}(MA_{0.15}FA_{0.85})_{0.95}Pb(I_{0.85}Br_{0.15})_3$ system, the incorporation of PECL on the surfaces was investigated using $FAPbI_3$ as a model system. The DFT-optimized lattice parameter of cubic $FAPbI_3$ is 6.360 Å. The surfaces were modeled with $FAPbI_3$(100) using slab models consisting of (3 × 3) supercells with a vacuum of 25 Å in the z-direction. All calculations are performed with the Vienna ab initio package (VASP).[4, 5] The total energy and forces are calculated within the framework of DFT, using the PBE exchange-correlation functional,[6] with the dispersion interaction corrected by the D3 scheme.[7] During the structural optimization, all ions and the part of PECL were allowed to relax. An energy cutoff of 400 eV and a k-point scheme of 3 × 3 × 1 were used to achieve energy and force convergence of 0.1 meV and 20 meV Å^{-1}, respectively.

Supplementary Note 1

The calculation of Vacancy Formation Energy

We calculate the formation energies of I and FA vacancies at the surface of the perovskite. Inspired by the previous reports[8-11], we define the suppression of I and FA vacancies formation due to the introduction of ionic groups (Cl^- and $N^+(CH_3)_3$). The details of the computational procedure are as follows:

$$\Delta E_{\mathrm{FA}vac} = \mathrm{E}\,[\mathrm{FA}vac] - \mathrm{E}\,[\mathrm{bulk}] + \mu\,[\mathrm{FA}] + \mathrm{E_F} \quad (1)$$

where E [FAvac] and E [bulk] are the total energies of the surfaces with and without FA vacancy, respectively, and E_F and μ [FA] are the Fermi energy and the chemical potential of FA, respectively. We assume that the E_F and μ [FA] are the same for all perovskites.

$$\Delta\Delta E_{\mathrm{FA}vac} = \Delta E_{\mathrm{FA}vac}\,[\mathrm{PECL}] - \Delta E_{\mathrm{FA}vac}\,[\mathrm{ref}] \quad (2)$$

where $\Delta E_{\mathrm{FA}vac}$ [PECL] is the formation energy of FA^+ vacancy in the presence of PECL, and $\Delta E_{\mathrm{FA}vac}$ [ref] is the pristine FAI-terminated surfaces. Moreover, the formula for calculating the $\Delta\Delta E_{\mathrm{I}vac}$ is consistent with the calculation of $\Delta\Delta E_{\mathrm{FA}vac}$.

Supplementary Note 2

The tDOS analysis method

The trap energy level (Ea) can be derived via the relation:

$$\omega_0 = \beta T^2 exp(\frac{-E_a}{k_B T}) \tag{3}$$

where ω_0 is the characteristic transition (attempt to escape) frequency, which can be defined from the peak value of the [-ω×dC/dω] curve.[12] β is temperature independent parameter, k_B is the Boltzmann's constant, and T is the temperature, respectively. According to this equation, the Arrhenius plot ($\ln(\frac{\omega_0}{T^2}) = \ln\beta - \frac{E_a}{k_B T}$), and the value of Ea can be obtained from the slope of the Arrhenius plot line.

The energetic profile of tDOS can be derived from the angular frequency-dependent capacitance using the equation:

$$N_T(E_\omega) = -\frac{V_{bi}\, dC\ \omega}{qWd\omega k_B T} \tag{4}$$

where V_{bi} is the built-in potential, W is the depletion width, ω is the angular frequency, k_B is the Boltzmann's constant, q is the elementary charge, T is the temperature, C is the capacitance. According to the depletion approximation, the C, V_{bi}, and W at the junction can be expressed in the relation, $\frac{C}{A} = \frac{\varepsilon\varepsilon_0 N}{W} = \sqrt{\frac{q\varepsilon\varepsilon_0 N}{2(V_{bi}-V)}}$, where A is the active area, ε is the static permittivity of perovskite, ε_0 is the permittivity of free space, N is the apparent doping profile in the depleted layer, and V is the applied bias. A Mott-Schottky plot ($\frac{A^2}{C^2} = \frac{2(V_{bi}-V)}{q\varepsilon\varepsilon_0 N}$) describes a straight line where the intersection on the bias axis determines V_{bi} and the slope gives the impurity doping density N. Then, the depletion width $W = \sqrt{\frac{2\varepsilon\varepsilon_0 V_{bi}}{qN}}$ corresponding to the zero bias can be calculated.

E_ω is the energy demarcation calculated from the angular frequency (ω):

$$E_\omega = k_B T \ln\frac{\omega_0}{\omega} \tag{5}$$

where ω_0 is the attempt-to-escape frequency.

Supplementary Note 3

The decay curves are fitted using a bi-exponential equation,

$$y = A_1 \exp\left[-\frac{x - x_0}{\tau_1}\right] + A_2 \exp\left[-\frac{x - x_0}{\tau_2}\right] \quad (6)$$

where τ_1 represents fast decay time, which is related to the trap-induced nonradiative recombination. τ_2 represents slow decay time, which is related to the radiative recombination in bulk perovskite.[13, 14] The fitted parameters are listed in **Table S1**.

Supplementary Note 4

J-V tests under different light intensity are calculated according to the following equation,[15]

$$V_{OC} = \frac{n_{id} k_B T}{q} ln(I) + B \quad (7)$$

where n_{id} is ideal factor, k_B is Boltzmann constant, T is absolute temperature, q is the lementary charge and B is the constant, respectively. We fit the data points with a slope of $n_{id}k_B T/q$. The larger the n_{id} value, the greater probability of trap-assisted recombination.

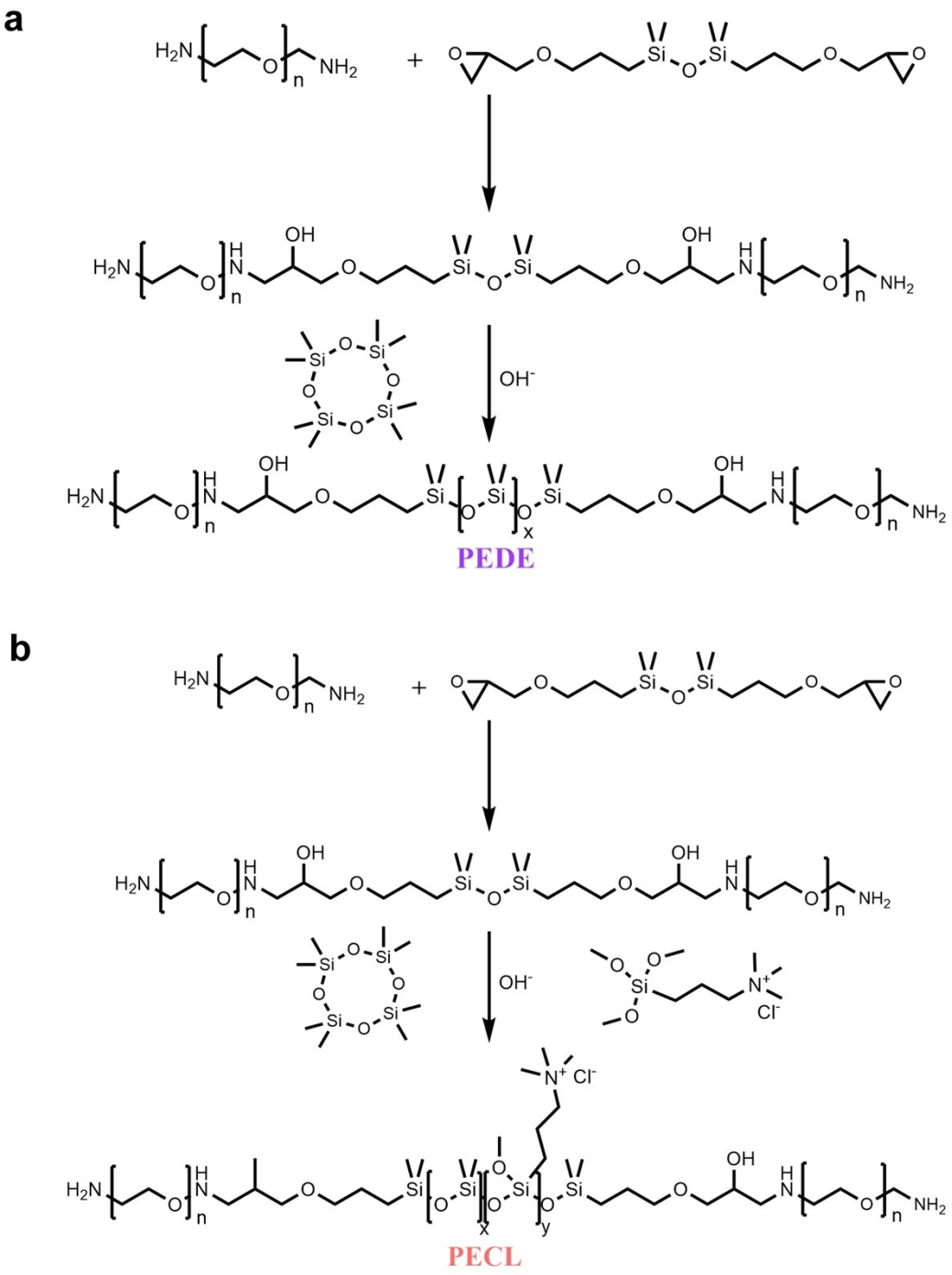

Figure S1. The synthetic routes of the (a) PEDE and (b) PECL polymer.

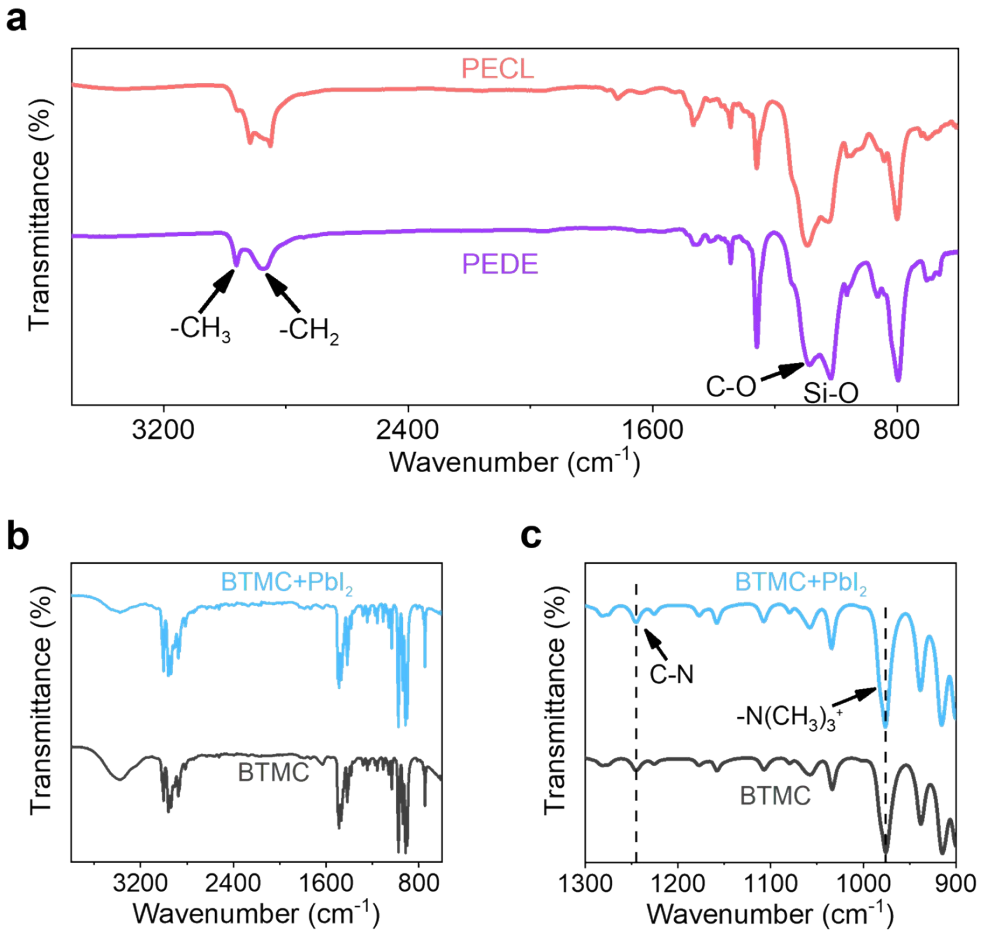

Figure S2. (a) FTIR spectra of PEDE and PECL polymer. (b)-(c) FTIR spectra of BTMC and BTMC-PbI_2 mixture.

The stretching vibration peak of -CH_3 and -CH_2- is observed at 2963 cm^{-1} and 2870 cm^{-1}. The peak at 1093 cm^{-1} is the stretching vibrations of C-O, while the stretching vibration peaks of Si-O are observed at 1018 cm^{-1}. The peak at 801 cm^{-1} is the stretching vibrations of Si-$(CH_3)_3$.[16] In addition, the peak at 976 cm^{-1} represents the quaternary ammonium group of BTMC, and another peak at 1244 cm^{-1} represents the C–N stretching vibration in **Figure S2b-c**.[17]

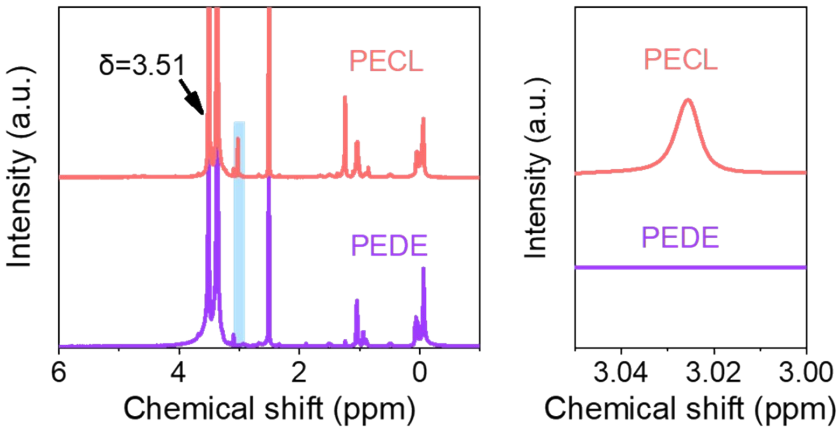

Figure S3. ^{1}H NMR spectra of the PEDE and PECL polymer.

The peak at δ=3.51 ppm is the proton peak of hydrogen on the C-O groups. The proton characteristic peak at δ=3.03 ppm is methyl groups in N $(-CH_3)_3^+$, suggesting that ionic groups have been successfully introduced into the polymer chain segment.[18]

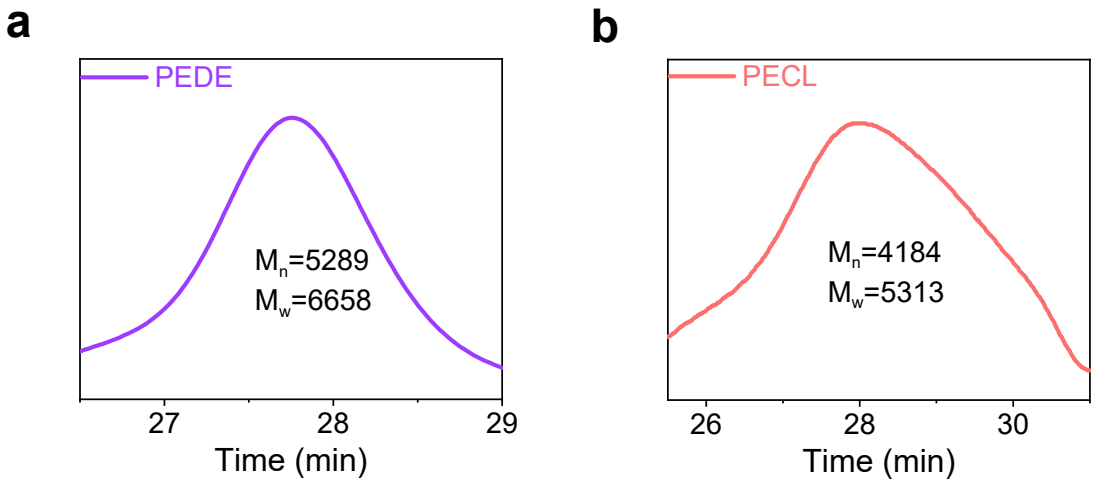

Figure S4. The gel permeation chromatography (GPC) curves of the PEDE and PECL polymer.

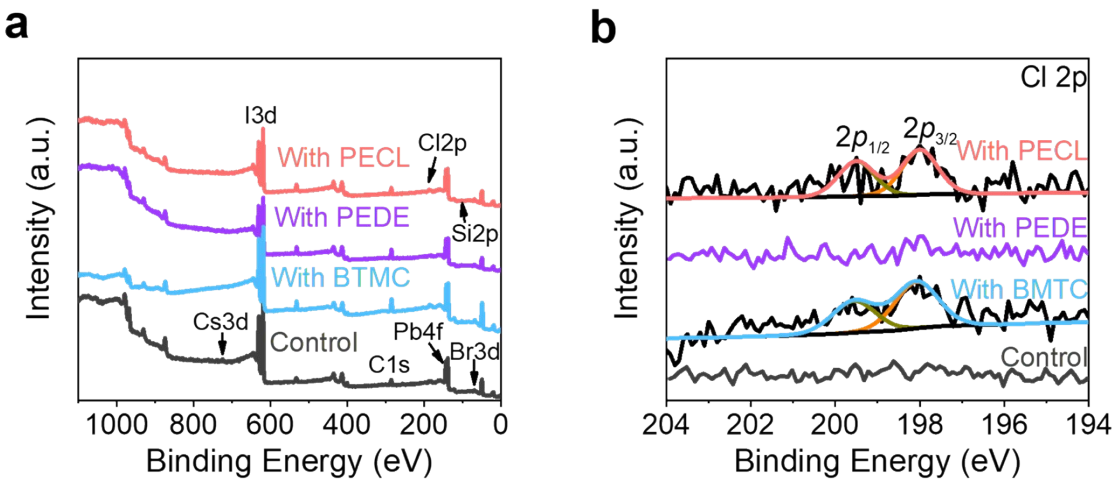

Figure S5. (a) XPS full spectra of the control, BTMC-, PEDE-, and PECL-modified perovskite film. (b) XPS spectra of Cl 2p of the control, BTMC-, PEDE-, and PECL-modified perovskite film.

As shown in **Figure S5b**, the Cl 2p signals appear at 198.0 eV and 199.5 eV in the BTMC- and PECL-modified perovskite film respectively, while PEDE-modified perovskite film does not exist in the Cl 2p signals, confirming that ionic groups have been successfully incorporated in the perovskite films.

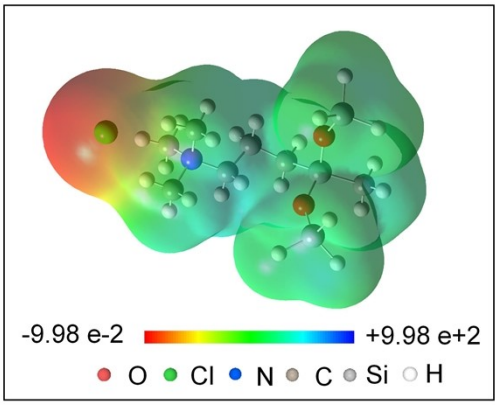

Figure S6. The electron distribution diagram of the ionic units in PECL polymer. The ionic groups are chosen to simplify the calculation.

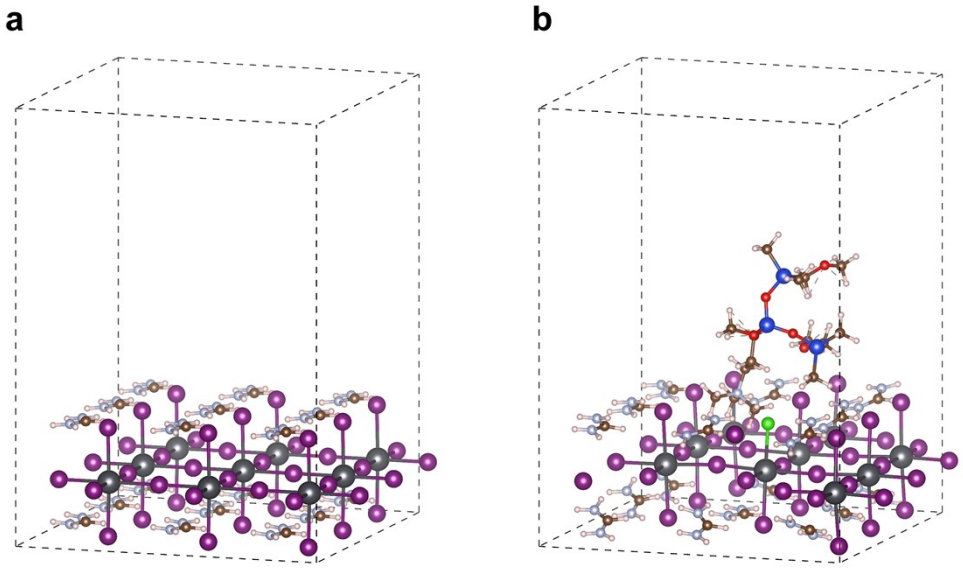

Figure S7. Theoretical calculations for the passivation mechanism of ionic groups. (a) The $FAPbI_3$ slab with a single layer, (b) Optimized structures of the ionic groups adjacent to the $FAPbI_3$.

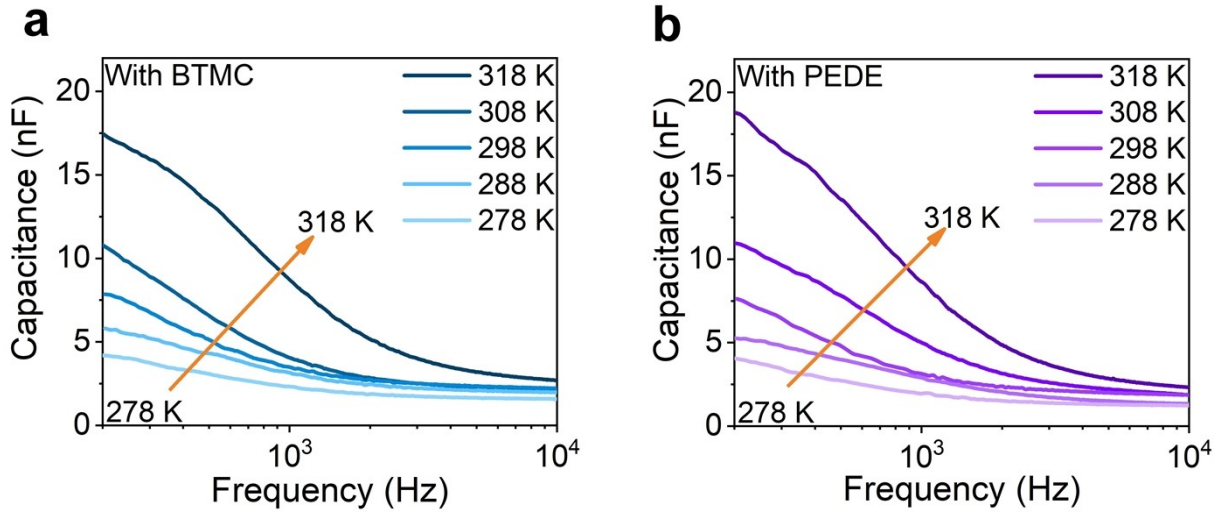

Figure S8. Temperature dependent capacitance spectra of the (a) BTMC- and (b) PEDE -modified devices.

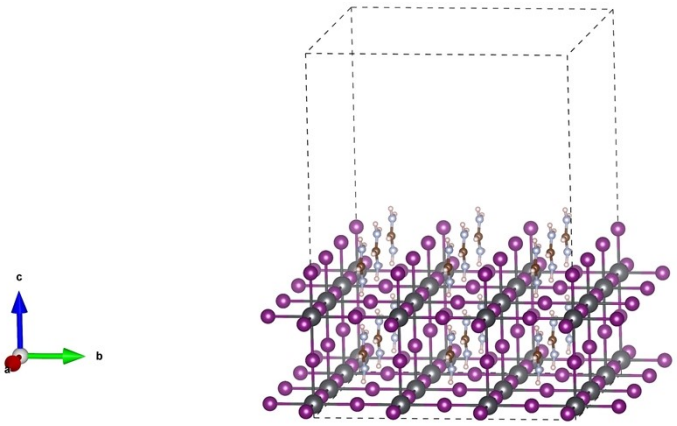

Figure S9. The $FAPbI_3$ slab model with the FA-termination.

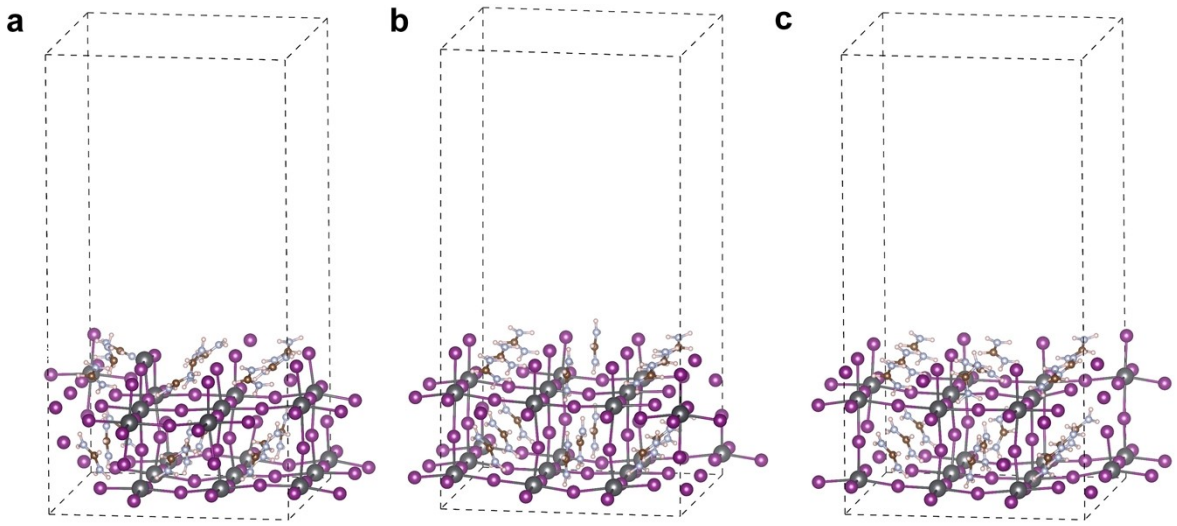

Figure S10. The $FAPbI_3$ slab with (a) a Pb cluster defect, (b) a FA-vacancy defect, and (c) an I-vacancy defect.

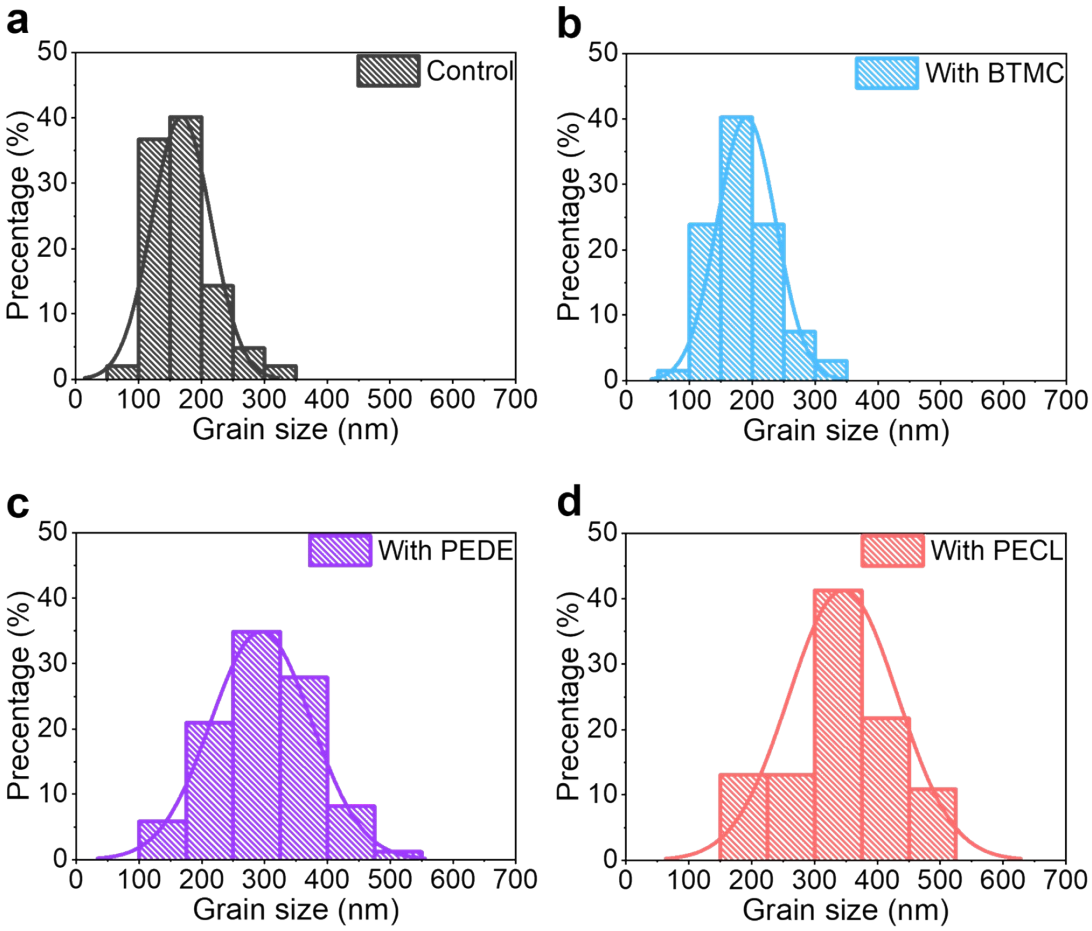

Figure S11. The distribution statistics of grain sizes of the (a) control, (b) BTMC-, (c) PEDE-, and (d) PECL-modified perovskite film.

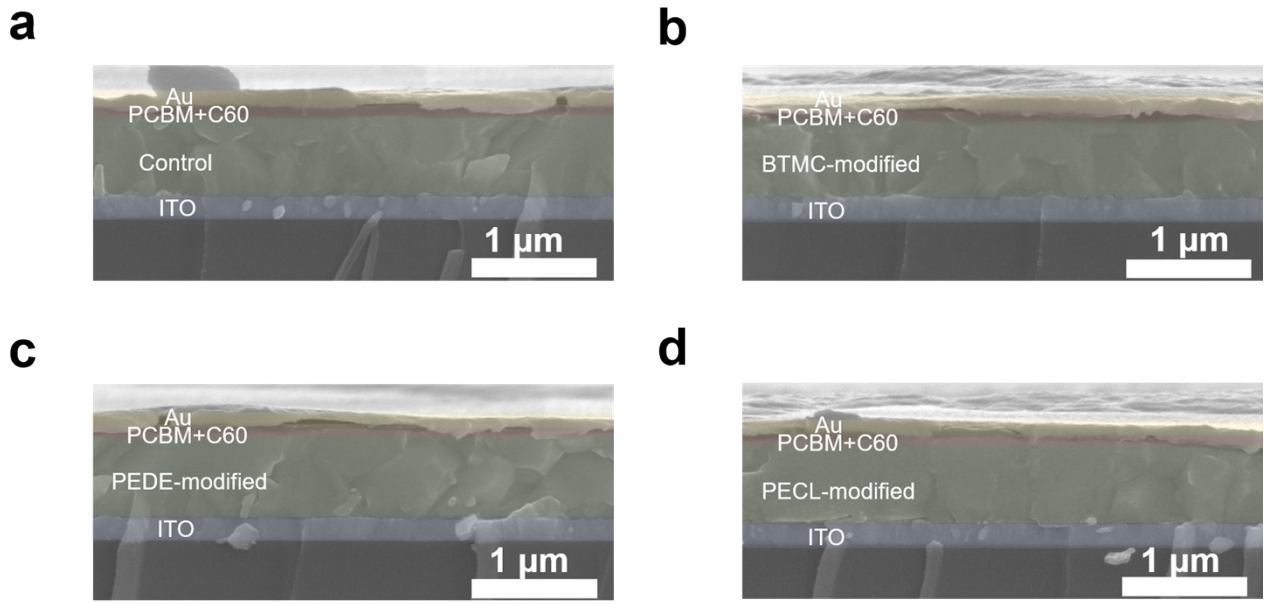

Figure S12. The cross-sectional SEM images of the (a) control, (b) BTMC-, (c) PEDE-, and (d) PECL-modified perovskite PSCs.

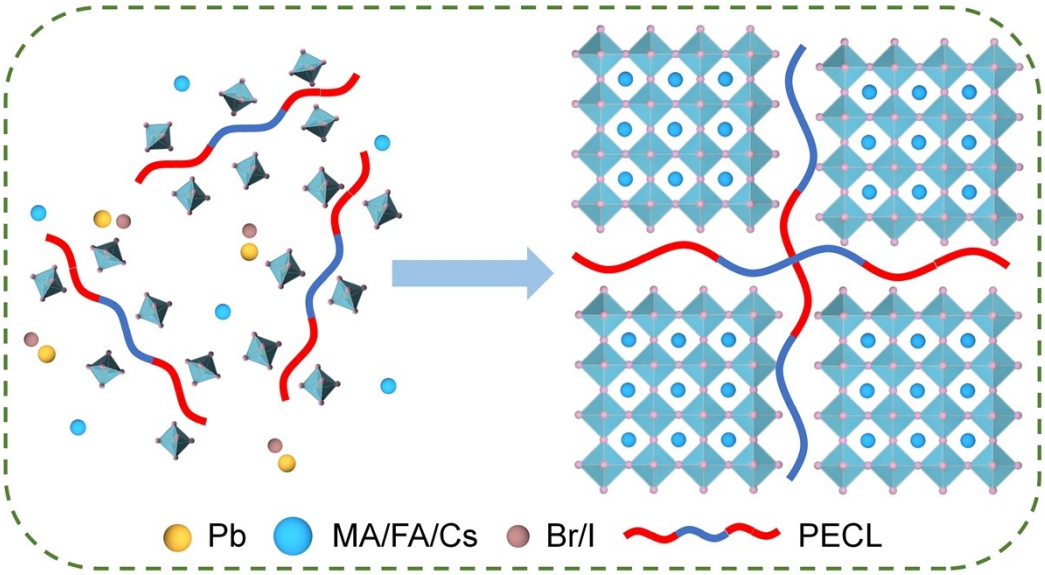

Figure S13. The cross-linking schematic diagram of perovskite grains with PECL polymer.

When the PECL polymer is incorporated in perovskite, the interaction between PECL and the perovskite ensures the immobilization of crystals grown in the vicinity of long-chain polymers due to the abundant oxygen sites on the PECL polymer. With the further growth of the crystals, the PECL polymer is squeezed into the GBs. Eventually, the PECL polymer achieves efficient cross-linking via direct backbone attachment. Thus, the abundant oxygen sites and the strong interaction are key to obtaining the cross-linking microstructure.

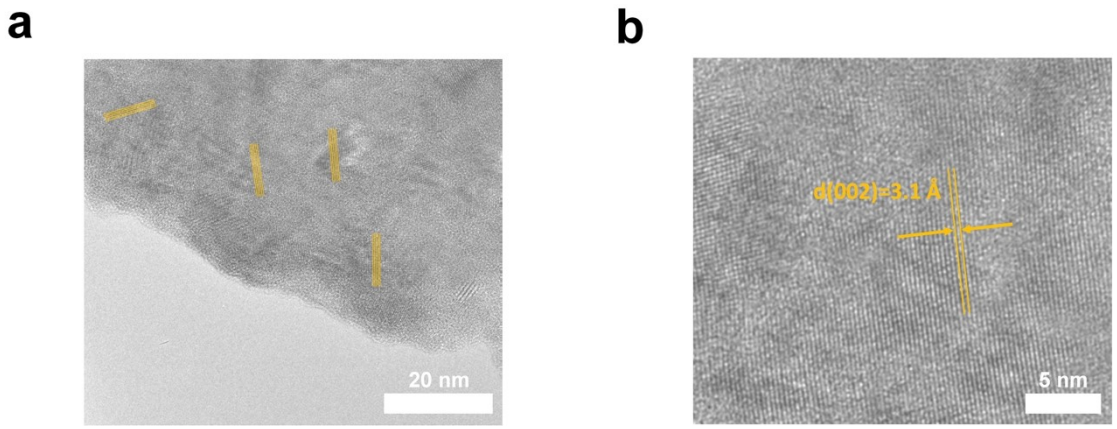

Figure S14. TEM image of control perovskite at (a) lower magnification and (b) higher magnification.

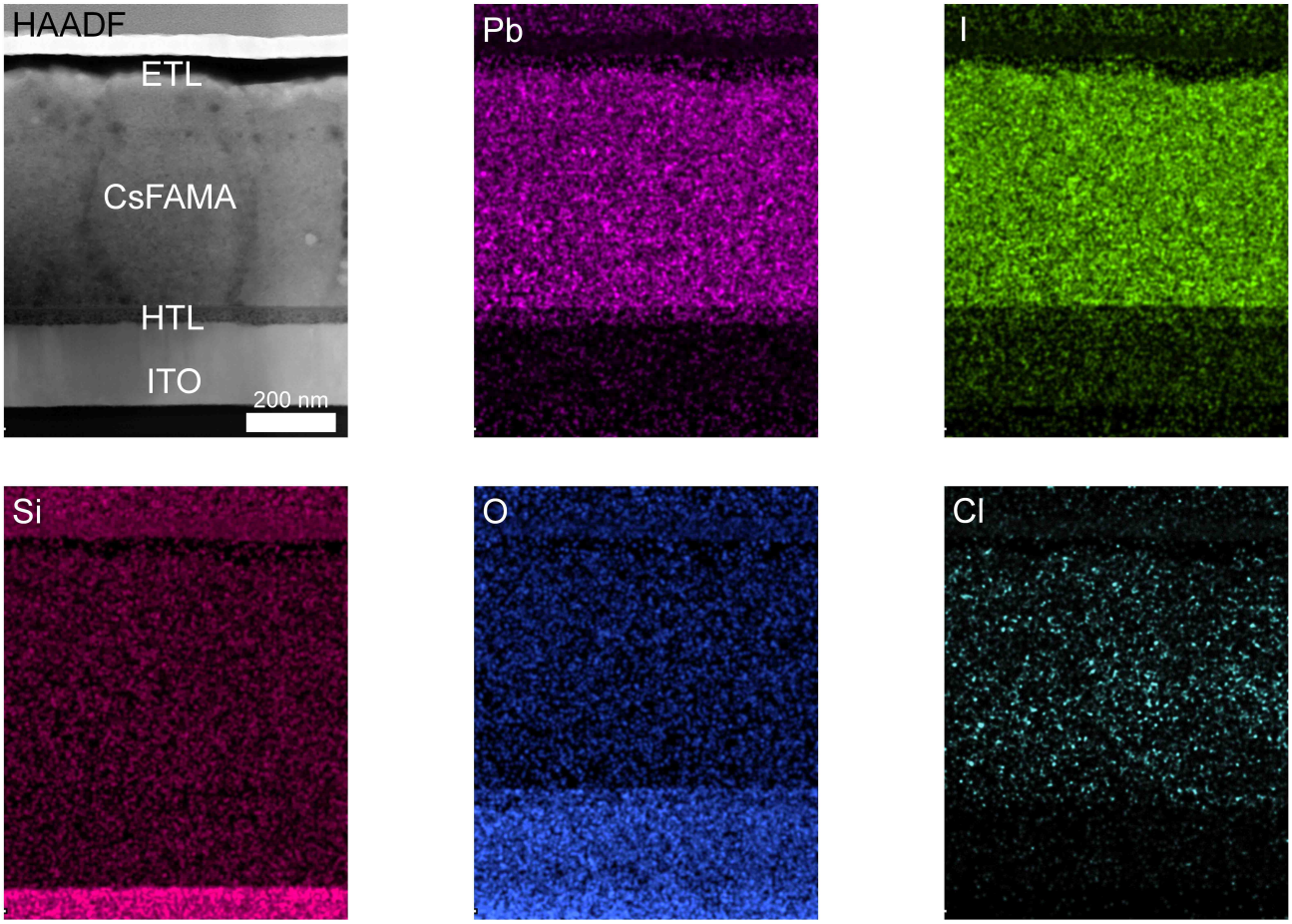

Figure S15. TEM-EDX mapping of the Pb, I, Si, O, and Cl elements in the cross section of PECL-modified PSCs.

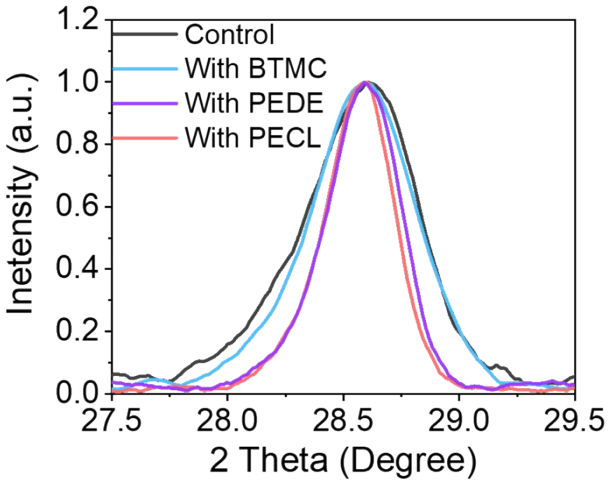

Figure S16. FWHM (the (220) diffraction peak) of the control, BTMC-, PEDE-, and PECL-modified perovskite film.

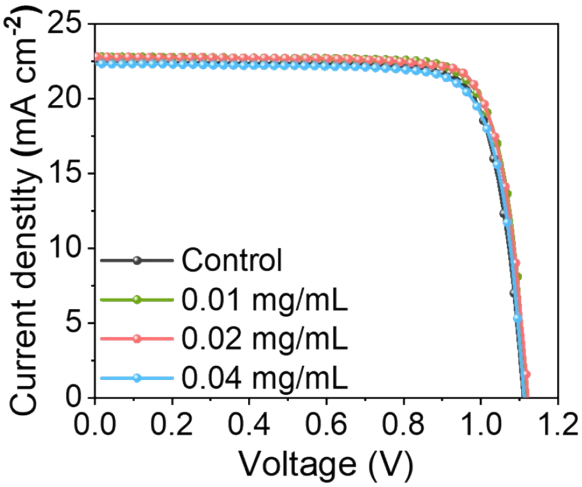

Figure S17. *J-V* curves of the BTMC-modified devices with different concentrations.

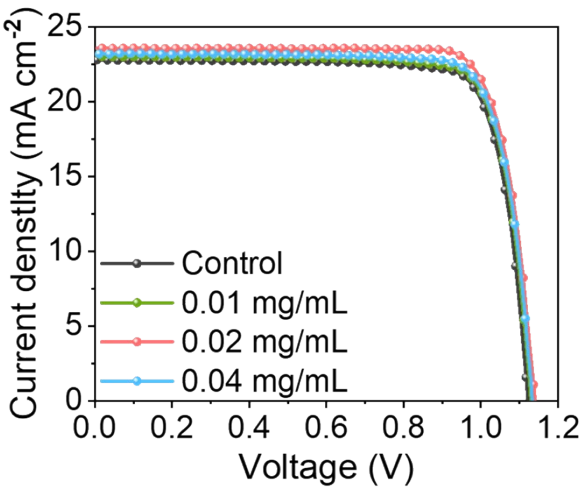

Figure S18. *J-V* curves of the PEDE-modified devices with different concentrations.

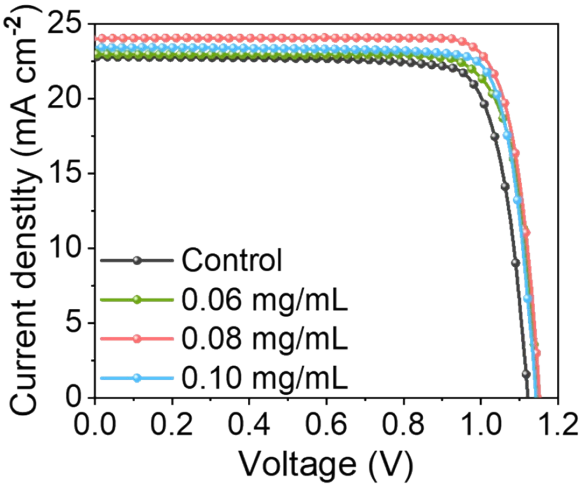

Figure S19. *J-V* curves of the PECL-modified devices with different concentrations.

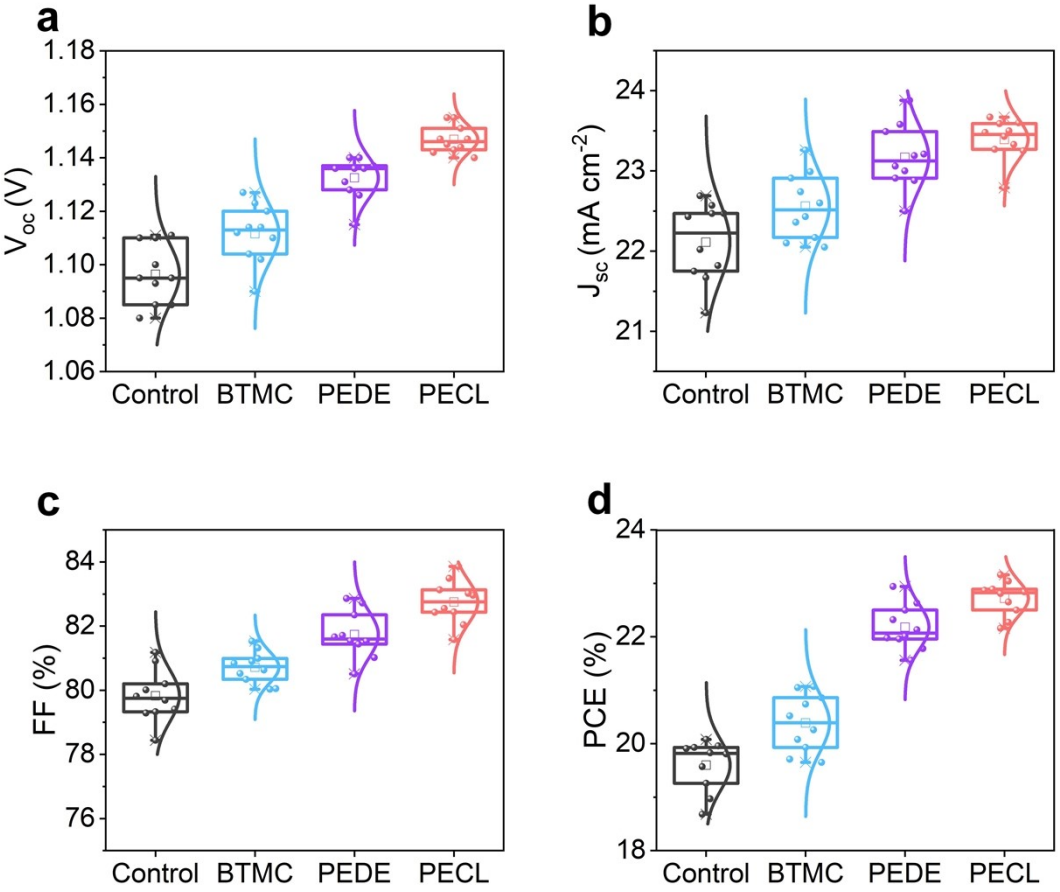

Figure S20. The statistical distribution of (a) V_{OC}, (b) J_{SC}, (c) FF, and (d) PCE for control, BTMC-, PEDE-, and PECL-modified PSCs (10 devices were collected from the different batches).

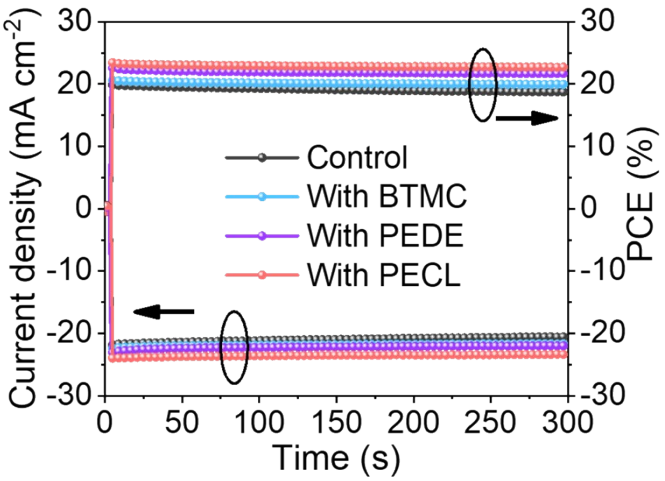

Figure S21. Steady current density and SPO values were measured under MPP for PSCs without and with additives. The bias voltage is 0.92 V (Control), 0.94 V (BTMC-modified), 0.97 V (PEDE-modified) and 0.98 V (PECL-modified), respectively.

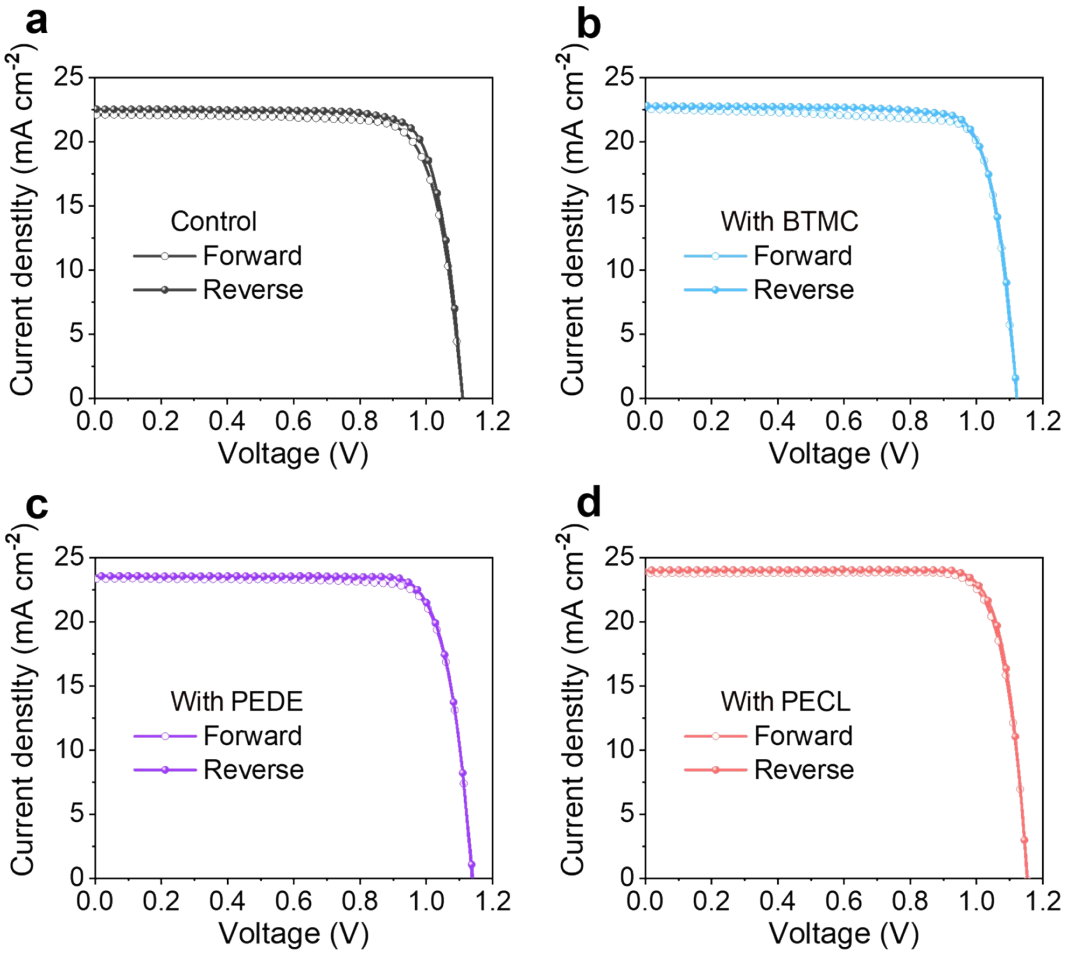

Figure S22. The reverse and forward *J-V* curves of the control, BTMC-, PEDE-, and PECL-modified PSCs.

The value of hysteresis index (*HI*) is defined as the formula,

$$HI = \frac{PCE_{Reverse} - PCE_{Forward}}{PCE_{Reverse}} \quad (8)$$

The summary of device performance is shown in **Table S5**. Compared with the hysteresis index (*HI*) of control (3.36%), BTMC- (2.34%), and PEDE- (2.21%), the *HI* of the PECL-modified device is reduced to 1.94%.

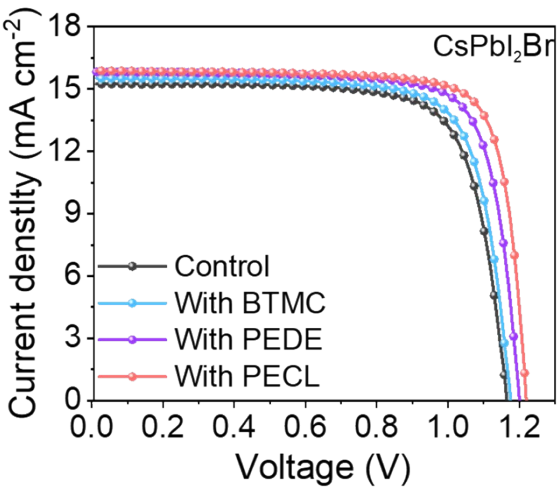

Figure S23. J-V curves of the control, BTMC-, PEDE-, and PECL-modified PSCs based on CsPbI2Br perovskite.

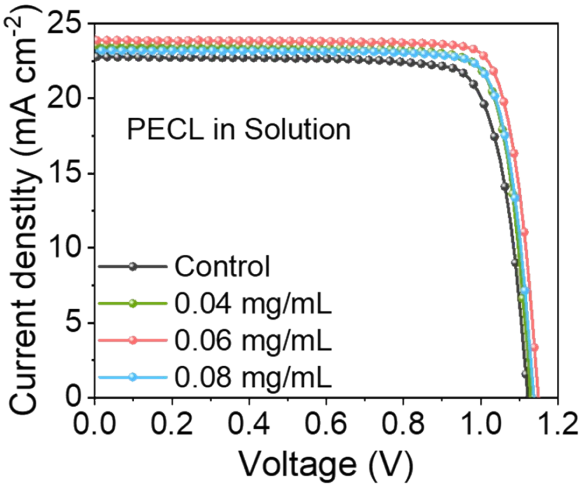

Figure S24. J-V curves of the PECL-modified devices with different concentrations via precursor solution method.

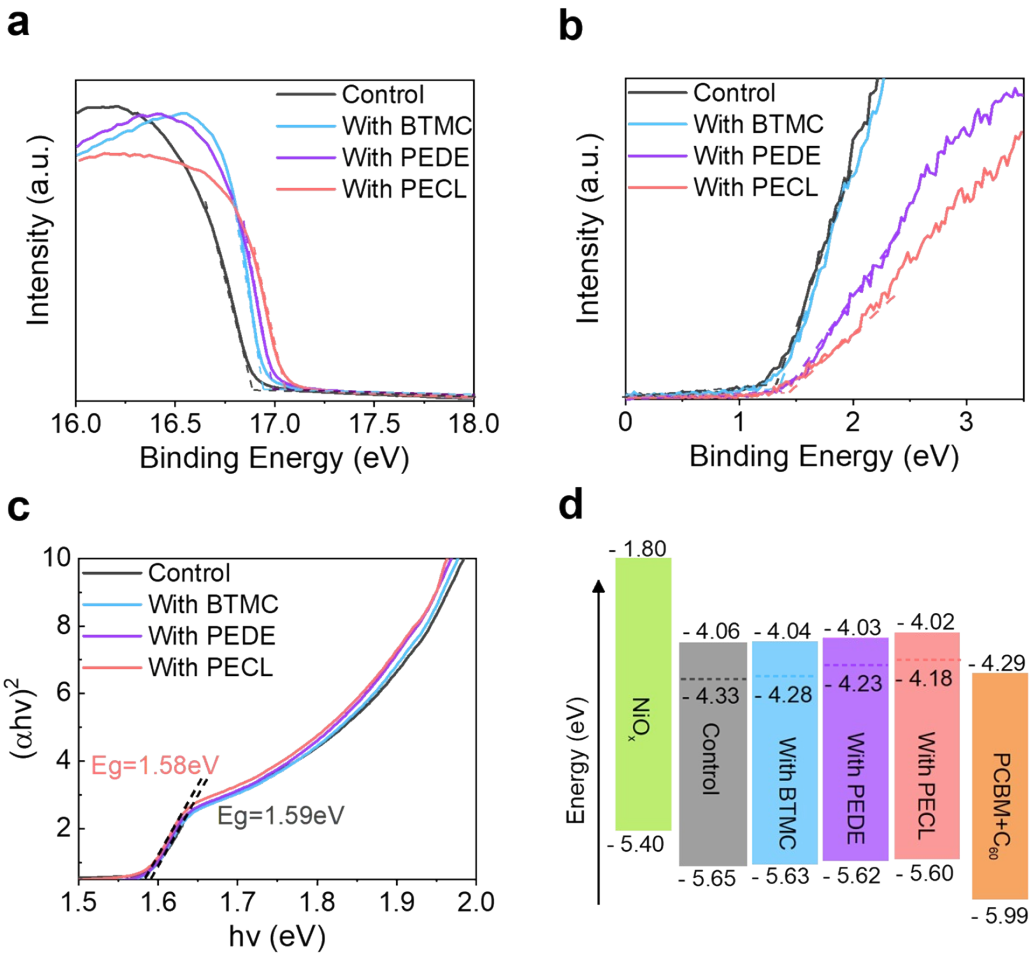

Figure S25. Energy-level characterization of the control and additives-modified perovskite films. (a) The secondary-electron cut-off plots. (b) Spectra in the valence band. (c) Tauc plots of the control and additives-modified perovskite films. The optical bandgap of control, BTMC-, PEDE-modified films remain similar (~1.59 eV), the optical bandgap of PECL-modified films is 1.58 eV. (d) The schematic energy level alignment of the perovskite films.

We calculate valence band maximum (VBM), conduction band minimum (CBM), and Fermi energy (E_F) levels of the control and additives-modified perovskite films from ultraviolet photoelectron spectra (UPS, **Figure S23a-b**) and tauc plot (**Figure S23c**). **Figure S23d** presents a schematic of the energy level scheme for the perovskite film with control and additives-modified. The VBM of additives-modified films exhibits slight changes to the control film, which has a better band alignment with the NiO_x hole transport layer.

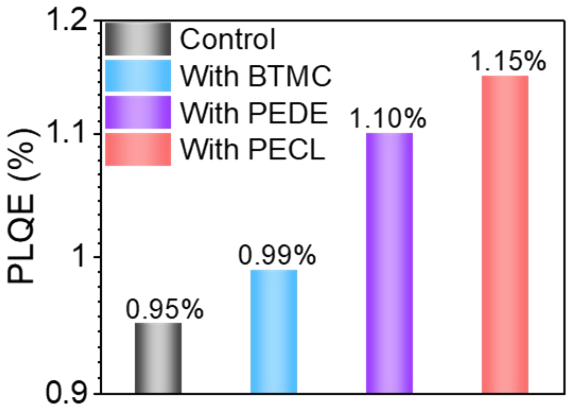

Figure S26. PLQE values of the control and additives-modified perovskite films.

The photoluminescence quantum efficiency (PLQE) of the additive-modified perovskite films is significantly enhanced compared with the control film. The PLQE of the control film is 0.95%, while PLQE of the BTMC-, PEDE-, and PECL-modified films are 0.99%, 1.10% and 1.15%, respectively. The increase in PLQE suggests that the additive-modified perovskite films exhibit suppressed nonradiative losses, leading to an increase in $V_{OC.}$

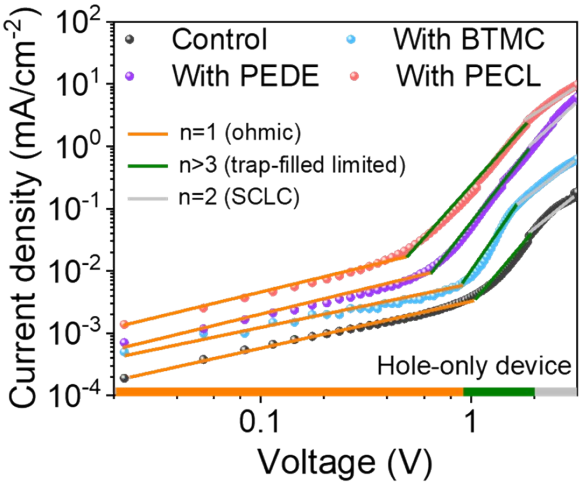

Figure S27. Charge extraction characteristics analysis of PSCs. *J-V* curves of the hole-only (ITO /NiO_x /control or additives-modified /spiro-MeOTAD /Au) devices.

The trap state density is derived from by trap-filled limiting voltage (V_{TFL}) using the equation,[19]

$$n_t = \frac{2\varepsilon_0 \varepsilon V_{TFL}}{qL^2} \tag{9}$$

where e is the electron charge, ε is the relative dielectric constant of perovskite (ε=25.5), ε_0 is the vacuum permittivity, and L is the thickness of perovskite film, and n_t is trap state density. V_{TFL} corresponds to the voltage at the intersection of the two *J-V* curves for the ohmic regime and the trap-filled regime. Therefore, the calculated n_t is 4.54×10^{15} cm^{-3} and 3.98×10^{15} cm^{-3} for the control and BTMC-modified device, while the n_t of PEDE-modified device and PECL-modified device is 2.84×10^{15} cm^{-3} and 2.30×10^{15} cm^{-3}, which directly illustrates that the PECL polymer additive can reduce perovskite defects.

The hole mobilities can be calculated according to the space charge limit current (SCLC) regions (n=2), the dark current is fitted by the Mott-Gurney law:

$$J = \frac{9}{8}\varepsilon\varepsilon_0\mu\frac{V^2}{L^3} \tag{10}$$

where J is the current, μ is the mobility, V is the applied bias voltage, ε is the relative permittivity of the perovskite, ε_0 is the vacuum permittivity, and the L is the thickness of the perovskite light-absorbing layer. The hole mobility of the PECL-modified device increases to 56.58 cm^2 V^{-1} s^{-1} from 35.87 cm^2 V^{-1} s^{-1} of the control, while the hole mobility of the BTMC- and PEDE-modified devices are 39.31 cm^2 V^{-1} s^{-1} and 49.49 cm^2 V^{-1} s^{-1}, demonstrating that the PECL polymer incorporated perovskite film is beneficial to accelerate carrier transport.

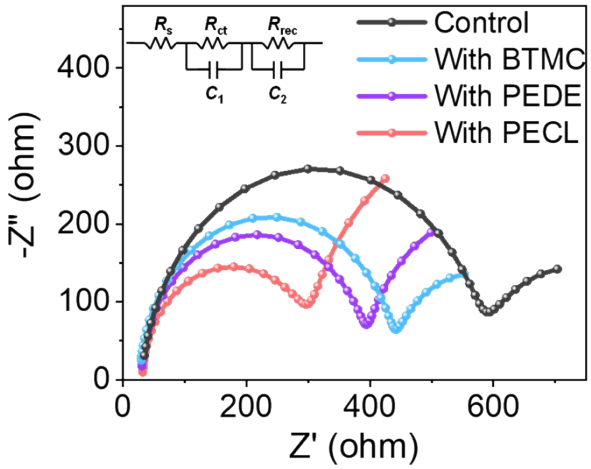

Figure S28. The Nyquist plots of the control, BTMC-, PEDE-, and PECL-modified devices in the dark state.

The high-frequency and low-frequency of the Nyquist plots correspond to the charge transport resistance (R_{ct}) and the recombination resistance (R_{rec}), respectively. According to the equivalent circuit, the fitting charge R_{ct} (R_{rec}) of control, BTMC-, PDED-, and PECL-modified devices are 593 Ω (344 Ω), 470 Ω (384 Ω), 394Ω (608 Ω), 306 Ω (852 Ω), respectively. The results indicate more efficient electron transport and less carrier recombination.

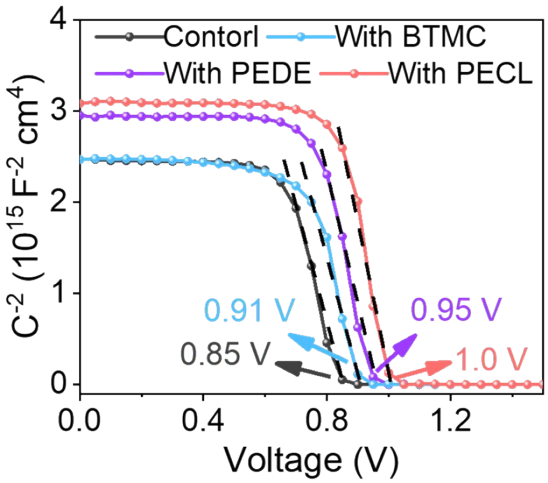

Figure S29. The Mott-Schottky plots of the control, BTMC-, PEDE-, and PECL-modified devices in the dark state.

The built-in potential (V_{bi}) is derived from the capacitance-voltage (C–V) curves by the Mott–Schottky equation,

$$\frac{1}{C^2} = \frac{2(V_{bi} - V)}{A^2 e\varepsilon\varepsilon_0 N_A} \tag{10}$$

where A is device area, ε is relative permittivity, ε_0 is vacuum permittivity, and N_A is carrier concentration. The built-in potential V_{bi} increases from 0.85 V (control) to 0.91 V (BTMC) and 0.95 V (PEDE), and then to 1 V (PECL).

Table S1. Fitting paraments of TRPL spectra of the control perovskite film, BTMC-modified perovskite film, PEDE-modified perovskite film, and PECL-modified perovskite film.

Sample	τ_1 [ns]	A_1 [%]	τ_2 [ns]	A_2 [%]	τ_{avg} [ns]
Control	3.30	85.40	235.40	14.60	217.81
With BTMC	4.21	68.93	261.88	31.07	253.00
With PEDE	7.64	49.80	278.26	50.20	271.08
With PECL	8.03	49.23	304.38	50.77	296.99

Table S2. Summary of device performance for BTMC-modified PSCs based on different concentrations. The devices were measured under 100 mW/cm^2 AM 1.5 G illumination. The scan rate is 0.1 V s^{-1}.

Concentration	V_{OC} [V]	J_{SC} [mA cm^{-2}]	FF [%]	PCE [%]
Control	1.11	22.51	80.15	20.02
0.01 mg/mL	1.12	22.82	80.21	20.50
0.02 mg/mL	1.12	22.79	81.03	20.68
0.04 mg/mL	1.11	22.33	79.49	19.70

Table S3. Summary of device performance for PEDE-modified PSCs based on different concentrations. The devices were measured under 100 mW/cm^2 AM 1.5 G illumination. The scan rate is 0.1 V s^{-1}.

Concentration	V_{OC} [V]	J_{SC} [mA cm^{-2}]	FF [%]	PCE [%]
Control	1.11	22.51	80.15	20.02
0.01 mg/mL	1.13	23.02	81.09	21.09
0.02 mg/mL	1.14	23.59	82.57	22.21
0.04 mg/mL	1.13	23.21	81.03	21.25

Table S4. Summary of device performance for PECL-modified PSCs based on different concentrations. The devices were measured under 100 mW/cm^2 AM 1.5 G illumination. The scan rate is 0.1 V s^{-1}.

Concentration	V_{OC} [V]	J_{SC} [mA cm^{-2}]	FF [%]	PCE [%]
Control	1.11	22.51	80.15	20.02
0.06 mg/mL	1.15	22.94	81.44	22.26
0.08 mg/mL	1.15	23.98	83.79	23.11
0.10 mg/mL	1.14	23.45	83.05	22.20

Table S5. Summary of device performance for control, BTMC, PEDE, and PECL-modified PSCs under reverse and forward scans. The devices were measured under 100 mW/cm^2 AM 1.5 G illumination. The scan rate is 0.1 V s^{-1}.

Device	Scanning mode	V_{OC} [V]	J_{SC} [mA cm^{-2}]	FF [%]	PCE [%]	HI [%]
Control	Forward	1.11	22.09	79.01	19.37	3.36
	Reverse	1.11	22.51	80.15	20.02	
With BTMC	Forward	1.12	22.46	80.34	20.21	2.34
	Reverse	1.12	22.79	81.03	20.68	
With PEDE	Forward	1.14	23.30	81.86	21.75	2.21
	Reverse	1.14	23.59	82.57	22.21	
With PECL	Forward	1.15	23.68	82.97	22.67	1.94
	Reverse	1.15	23.98	83.79	23.11	

Table S6. Device performance summary for the control, BTMC-, PEDE-, and PECL-modified PSCs based on $CsPbI_2Br$ perovskite. The devices were measured under 100 mW/cm^2 AM 1.5 G illumination. The scan rate is 0.1 V s^{-1}.

Device	V_{OC} [V]	J_{SC} [mA cm^{-2}]	FF [%]	PCE [%]
Control	1.16	15.25	75.34	13.37
With BTMC	1.17	15.53	76.20	13.85
With PEDE	1.20	15.82	77.85	14.78
With PECL	1.22	15.88	79.88	15.45

Table S7. Summary of device performance for PECL-modified PSCs based on different concentrations via precursor solution method. The devices were measured under 100 mW/cm^2 AM 1.5 G illumination. The scan rate is 0.1 V s^{-1}.

Device	V_{OC} [V]	J_{SC} [mA cm^{-2}]	FF [%]	PCE [%]
Control	1.11	22.51	80.15	20.02
0.04 mg/mL	1.13	23.56	82.64	22.00
0.06 mg/mL	1.15	23.88	83.72	22.99
0.08 mg/mL	1.15	23.18	83.22	22.18

Table S8. Specific values of charge transport resistance (R_{ct}), and recombination resistance (R_{rec}) of PSCs based additives-modified perovskite.

Device	Charge transport resistance (R_{ct})	Recombination resistance (R_{rec})
Control	593 Ω	344 Ω
With BTMC	470 Ω	384 Ω
With PEDE	394Ω	608 Ω
With PECL	306 Ω	852 Ω

References

1. S. Wang, Y. Li, J. Yang, T. Wang, B. Yang, Q. Cao, X. Pu, L. Etgar, J. Han, J. Zhao, X. Li and A. Hagfeldt, *Angew. Chem. Int. Ed.*, 2022, **61**, e202116534.
2. M. Zhang, T. Li, J. Yu, G. Lu, H. Zhou and X. Zhan, *Sol. RRL*, 2020, **4**, 2000140.
3. S. Wang, B. Yang, J. Han, Z. He, T. Li, Q. Cao, J. Yang, J. Suo, X. Li, Z. Liu, S. Liu, C. Tang and A. Hagfeldt, *Energy Environ. Sci.*, 2020, **13**, 5068-5079.
4. G. Kresse and J. Hafner, *Phys. Rev. B*, 1994, **49**, 14251-14269.
5. G. Kresse and J. Furthmüller, *Comput. Mater. Sci.*, 1996, **6**, 15-50.
6. J. P. Perdew, K. Burke and M. Ernzerhof, *Phys. Rev. Lett.*, 1996, **77**, 3865-3868.
7. K. Kowalski, S. Krishnamoorthy, O. Villa, J. R. Hammond and N. Govind, *J. Chem. Phys.*, 2010, **132**, 154103.
8. M. I. Saidaminov, J. Kim, A. Jain, R. Quintero-Bermudez, H. Tan, G. Long, F. Tan, A. Johnston, Y. Zhao, O. Voznyy and E. H. Sargent, *Nat. Energy*, 2018, **3**, 648-654.
9. H. Xie, Z. Wang, Z. Chen, C. Pereyra, M. Pols, K. Gałkowski, M. Anaya, S. Fu, X. Jia, P. Tang, D. J. Kubicki, A. Agarwalla, H.-S. Kim, D. Prochowicz, X. Borrisé, M. Bonn, C. Bao, X. Sun, S. M. Zakeeruddin, L. Emsley, J. Arbiol, F. Gao, F. Fu, H. I. Wang, K.-J. Tielrooij, S. D. Stranks, S. Tao, M. Grätzel, A. Hagfeldt and M. Lira-Cantu, *Joule*, 2021, **5**, 1246-1266.
10. N. Li, S. Tao, Y. Chen, X. Niu, C. K. Onwudinanti, C. Hu, Z. Qiu, Z. Xu, G. Zheng, L. Wang, Y. Zhang, L. Li, H. Liu, Y. Lun, J. Hong, X. Wang, Y. Liu, H. Xie, Y. Gao, Y. Bai, S. Yang, G. Brocks, Q. Chen and H. Zhou, *Nat. Energy*, 2019, **4**, 408-415.
11. H. Xie, Z. Wang, Z. Chen, C. Pereyra, M. Pols, K. Gałkowski, M. Anaya, S. Fu, X. Jia, P. Tang, D. J. Kubicki, A. Agarwalla, H.-S. Kim, D. Prochowicz, X. Borrisé, M. Bonn, C. Bao, X. Sun,

S. M. Zakeeruddin, L. Emsley, J. Arbiol, F. Gao, F. Fu, H. I. Wang, K.-J. Tielrooij, S. D. Stranks, S. Tao, M. Grätzel, A. Hagfeldt and M. Lira-Cantu, *Joule*, 2021, **5**, 1246-1266.

12. X. Meng, C. H. Y. Ho, S. Xiao, Y. Bai, T. Zhang, C. Hu, H. Lin, Y. Yang, S. K. So and S. Yang, *Nano Energy*, 2018, **52**, 300-306.

13. T. H. Han, J. W. Lee, C. Choi, S. Tan, C. Lee, Y. Zhao, Z. Dai, N. De Marco, S. J. Lee, S. H. Bae, Y. Yuan, H. M. Lee, Y. Huang and Y. Yang, *Nat. Commun.*, 2019, **10**, 520.

14. W. S. Yang, B.-W. Park, E. H. Jung, N. J. Jeon, Y. C. Kim, D. U. Lee, S. S. Shin, J. Seo, E. K. Kim, J. H. Noh and S. I. Seok, *Science*, 2017, **356**, 1376.

15. X. Zhu, M. Du, J. Feng, H. Wang, Z. Xu, L. Wang, S. Zuo, C. Wang, Z. Wang, C. Zhang, X. Ren, S. Priya, D. Yang and S. Liu, *Angew. Chem. Int. Ed.*, 2021, **60**, 4238-4244.

16. D. Cai, A. Neyer, R. Kuckuk and H. M. Heise, *J. Mol. Struct.*, 2010, **976**, 274-281.

17. M. Saha, M. S. Rahman, M. N. Hossain, D. E. Raynie and M. A. Halim, *J. Phys. Chem. A*, 2020, **124**, 4690-4699.

18. I. Delso, C. Lafuente, J. Muñoz-Embid and M. Artal, *J. Mol. Liq.*, 2019, **290**, 111236.

19. Y. Yang, J. Wu, X. Wang, Q. Guo, X. Liu, W. Sun, Y. Wei, Y. Huang, Z. Lan, M. Huang, J. Lin, H. Chen and Z. Wei, *Adv. Mater.*, 2019, **32**, 1904347.